Human Dystrophin Structural Changes upon Binding to Anionic Membrane Lipids

Raphael dos Santos Morais, Olivier Delalande, Javier Perez, Dominique Mias-Lucquin, Mélanie Lagarrigue, Anne Martel, Anne-Elisabeth Molza, Angélique Chéron, Céline Raguénès-Nicol, Thomas Chenuel, et al.

Dear author,

Please note that changes made in the online proofing system will be added to the article before publication but are not reflected in this PDF.

We also ask that this file not be used for submitting corrections.

Please cite this article in press as: Dos Santos Morais et al., Human Dystrophin Structural Changes upon Binding to Anionic Membrane Lipids, Biophysical Journal (2018), https://doi.org/10.1016/j.bpj.2018.07.039

Biophysical *Journal*
Article

Biophysical Society

Human Dystrophin Structural Changes upon Binding to Anionic Membrane Lipids

Raphael Dos Santos Morais,[1,2,3,4] Olivier Delalande,[1,2] Javier Pérez,[4] Dominique Mias-Lucquin,[1,2] Mélanie Lagarrigue,[1,5] Anne Martel,[6] Anne-Elisabeth Molza,[1,2] Angélique Chéron,[1,2] Céline Raguénès-Nicol,[1,2] Thomas Chenuel,[1,2] Arnaud Bondon,[7] Marie-Sousai Appavou,[8] Elisabeth Le Rumeur,[1,2] Sophie Combet,[3,*] and Jean-François Hubert[1,2,*]

[1]Université de Rennes, Rennes, France; [2]Institut de Génétique et Développement de Rennes, CNRS UMR 6290, Rennes, France; [3]Laboratoire Léon-Brillouin, UMR 12 CEA-CNRS, Université Paris-Saclay, CEA-Saclay, Gif-sur-Yvette, France; [4]SWING Beamline, Synchrotron SOLEIL, L'Orme des Merisiers, Saint-Aubin, Gif-sur-Yvette, France; [5]Inserm U1085, Protim-Plate-forme Protéomique, Rennes, France; [6]Institut Laue-Langevin, Grenoble, France; [7]CNRS 6226, Institut des Sciences Chimiques de Rennes, PRISM, Rennes, France; and [8]Jülich Centre for Neutron Science at Heinz Maier-Leibnitz Zentrum, Forschungszentrum Jülich GmbH, Garching, Germany

ABSTRACT Scaffolding proteins play important roles in supporting the plasma membrane (sarcolemma) of muscle cells. Among them, dystrophin strengthens the sarcolemma through protein-lipid interactions, and its absence due to gene mutations leads to the severe Duchenne muscular dystrophy. Most of the dystrophin protein consists of a central domain made of 24 spectrin-like coiled-coil repeats (R). Using small angle neutron scattering (SANS) and the contrast variation technique, we specifically probed the structure of the three first consecutive repeats 1–3 (R1–3), a part of dystrophin known to physiologically interact with membrane lipids. R1–3 free in solution was compared to its structure adopted in the presence of phospholipid-based bicelles. SANS data for the protein/lipid complexes were obtained with contrast-matched bicelles under various phospholipid compositions to probe the role of electrostatic interactions. When bound to anionic bicelles, large modifications of the protein three-dimensional structure were detected, as revealed by a significant increase of the protein gyration radius from 42 ± 1 to 60 ± 4 Å. R1–3/anionic bicelle complexes were further analyzed by coarse-grained molecular dynamics simulations. From these studies, we report an all-atom model of R1–3 that highlights the opening of the R1 coiled-coil repeat when bound to the membrane lipids. This model is totally in agreement with SANS and click chemistry/mass spectrometry data. We conclude that the sarcolemma membrane anchoring that occurs during the contraction/elongation process of muscles could be ensured by this coiled-coil opening. Therefore, understanding these structural changes may help in the design of rationalized shortened dystrophins for gene therapy. Finally, our strategy opens up new possibilities for structure determination of peripheral and integral membrane proteins not compatible with different high-resolution structural methods.

Q1 INTRODUCTION

Obtaining the structural information of membrane proteins is very challenging because of the difficulties associated with their handling (1). Only ~770 membrane protein structures have been made available (http://blanco.biomol.uci.edu/mpstruc/), and this number is considerably less than the numerous structures obtained for soluble proteins (2). Furthermore, for membrane proteins not compatible with x-ray crystallography, NMR, and/or the increasingly used cryo-electron microscopy (3), the challenge could be even trickier. To overcome this, small angle x-ray or neutron scattering (SAXS or SANS, respectively) are alternative techniques to obtain structural information on biological macromolecules either free in solution or bound to various partners (4) such as membrane proteins (5,6). The SANS-based contrast variation technique (7) allows us to specifically obtain low-resolution structures of proteins involved in macromolecular complexes and has been successfully applied to protein-polymer (8), protein-protein (7), protein-DNA/RNA (9,10), and protein-lipid/detergent complexes (11–13). We highlighted recently that phospholipid-based bicelles can be contrast matched to be used in SANS experiments as a relevant membrane mimic to probe conformational modifications of peripheral membrane proteins in interaction with phospholipids (14). In our

Submitted April 20, 2018, and accepted for publication July 31, 2018.

*Correspondence: sophie.combet@cea.fr or jfhubert@univ-rennes1.fr

Raphael Dos Santos Morais's present address is UMR 7365 CNRS-UL IMoPA, F-54505 Vandoeuvre-lès-Nancy, France.

Anne-Elisabeth Molza's present address is CNRS UPR 9080, Université Paris-Diderot, Sorbonne Paris Cité, F-75005 Paris, France.

Editor: Georg Pabst.

https://doi.org/10.1016/j.bpj.2018.07.039

Please cite this article in press as: Dos Santos Morais et al., Human Dystrophin Structural Changes upon Binding to Anionic Membrane Lipids, Biophysical Journal (2018), https://doi.org/10.1016/j.bpj.2018.07.039

study, this approach was developed to explore the structure-function relationship of a protein associated with severe genetic diseases, i.e., dystrophin (Fig. 1 *A*), a peripheral scaffolding membrane protein essential to protect muscle cell membrane (sarcolemma) against shear stresses (15). Indeed, its absence leads to the severe Duchenne muscular dystrophy (16), with an incidence of ~1 in 5000 male births (17).

Dystrophin consists mainly of a central domain that accounts for 75% of the protein sequence and has the particularity to be made of 24 spectrin-like repeats (denoted R1–R24) (Fig. 1 *B*). This protein is able to interact directly with the lipid part of the sarcolemma (18,19). In vitro experiments showed that the region from R1 to R19 is able to bind phospholipids (20,21). Recently, in vivo experiments highlighted that R1–3 is exclusively localized at the sarcolemma (19). Combination of these observations led to the conclusion that interactions of the central domain of dystrophin with membrane lipids must be considered for understanding its crucial scaffolding role in muscle cells. In particular, during the contraction process of muscles, the sarcolemma bends and areas containing invaginations are formed (22). These regions present a high degree of curvature, leading to a local lipid-packing defect. The influence of this phenomenon on the dystrophin/lipid interactions has been investigated with liposomes of various sizes (18). Our previous works highlighted that the interfacial properties of dystrophin are modulated according to the region of the protein involved (23), the nature of lipids, and the lipid packing (20,21), which all play key roles in the physiology of muscle cells. Moreover, the R1–3 protein fragment is bordered by two nonstructured hinges and is found in several potentially therapeutic shortened dystrophins, making it a relevant protein subdomain (24,25).

By combining SAXS and molecular modeling, we recently proposed solution structures of fragments of the central domain, including the R1–3 fragment (26). We obtained evidence of the conformation adopted by these protein fragments free in solution. However, an exhaustive knowledge of the structure of the dystrophin central domain, either alone or in interaction with membrane phospholipids, must be considered for understanding its crucial scaffolding role in muscle cells and also for helping in the design of therapeutic proteins.

In our study, we probed the three-dimensional (3D) structure of the R1–3 dystrophin lipid-binding fragment either free in solution or in interaction with zwitterionic or anionic bicelles made of DMPC/DHPC (dimyristoylphosphatidylcholine/dihexanoylphosphatidylcholine) or DMPC/DMPS (dimyristoylphosphatidylserine)/DHPC, respectively. Phosphatidylcholine (PC) and phosphatidylserine (PS) phospholipids are both well represented in the sarcolemma (27). PC is the most abundant phospholipid in the inner leaflet, representing 45% of the total phospholipids, whereas phosphatidylethanolamine (PE) and PS represent 23 and 18%, respectively, and the presence of unsaturated fatty acids contributes to the packing defects that are observed in plasma membranes (27–30). Within the bicelles, the structure of the torus is made of short fatty acids, which reproduces the lipid-packing defects of native sarcolemma. These considerations make the phospholipid-based bicelles relevant membrane mimics for both electrostatic and lipid-packing properties (14). Using a combination of SANS, click chemistry/mass spectrometry (MS), coarse-grained molecular dynamics (CG-MD), and interactive CG-MD (CG-IMD) simulations, we show that the tertiary structure of R1–3 is maintained upon binding to zwitterionic phospholipids, whereas in the presence of anionic phospholipids, R1–3 exhibits significant conformational modifications. We report an all-atom model of R1–3 in interaction with anionic membrane phospholipids, in which its structural changes are attributed to an opening of the coiled coil of repeat 1 (R1).

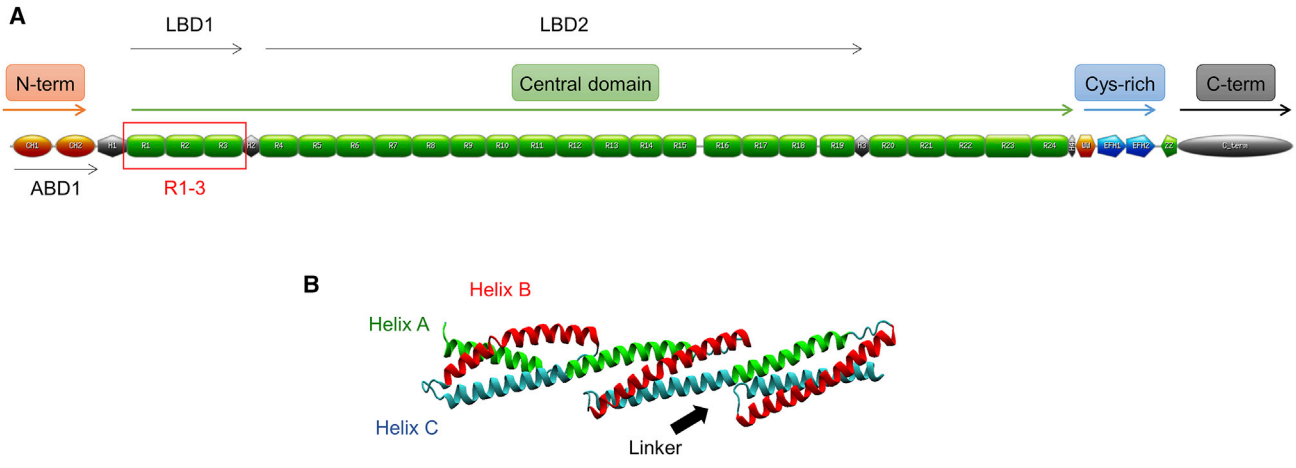

Web 3C

FIGURE 1 (*A*) Schematic representation of dystrophin and its four domains, including the central domain composed of 24 spectrin-like repeats (R). The R1–3 protein fragment is framed in red and can interact with membrane phospholipids. LBD, lipid binding domain; ABD, actin binding domain. (*B*) The 3D structure of three spectrin repeats folded in triple coiled coil (PDB: 1U4Q) showing the organization of dystrophin central domain is shown. The linker region is the junction between the helix C of one repeat and the helix A of the subsequent one. To see this figure in color, go online.

Please cite this article in press as: Dos Santos Morais et al., Human Dystrophin Structural Changes upon Binding to Anionic Membrane Lipids, Biophysical Journal (2018), https://doi.org/10.1016/j.bpj.2018.07.039

MATERIALS AND METHODS

Protein purification

R1–3 (333 residues, human dystrophin (Uniprot P11532) *GS*EVNLD…QISQA, the residues in italics being from the thrombin cleavage site) was designed according to the alignment of Winder et al. (31). R1–3 was expressed and purified as previously described with small modifications (21,32). Briefly, the His-tagged protein was produced in the BL21 *Escherichia coli* (DE3) strain and purified by immobilized metal affinity chromatography on Ni-Sepharose column (HisTrap; GE Healthcare, Chicago, IL) according to the manufacturer's instructions. The tag was removed by thrombin cleavage, and the protein was further purified with a size-exclusion chromatography column (HiLoad 16/600 Superdex 200 prep grade; GE Healthcare) equilibrated with TNE buffer (20 mM Tris, 150 mM NaCl, and 0.1 mM EDTA (pH 7.5)). The purity was assessed by sodium dodecyl sulfate-polyacrylamide gel electrophoresis (SDS-PAGE) stained with Coomassie blue (InstantBlue; Expedeon, Heidelberg, Germany), and the concentration was determined spectrophotometrically using a molar extinction coefficient at 280 nm of 59,720 $M^{-1} \cdot cm^{-1}$ and a molecular weight of 38.5 kDa (21). Buffer exchange for SANS experiments was performed by three successive diafiltrations with Amicon Ultra-15 or Ultra-4 (MWCO 10 kDa; Millipore, Burlington, MA), followed by an ultimate step with a desalting column (NAP5; GE Healthcare) to ensure a perfect buffer exchange.

Bicelle preparation

1,2-dimyristoyl-sn-glycero-3-phosphocholine (DMPC), 1,2-dimyristoyl-sn-glycero-3-phospho-L-serine (DMPS), 1,2-dihexanoyl-sn-glycero-3-phosphocholine (DHPC), 1,2-dimyristoyl-d54-sn-glycero-3-phosphocholine-1,1,2,2-d4-N,N,N-trimethyl-d9 (DMPC-d67), 1,2-dimyristoyl-d54-sn-glycero-3-[phospho-L-serine] (DMPS-d54), and 1,2-dihexanoyl-d22-sn-glycero-3-phosphocholine-1,1,2,2-d4-N,N,N-trimethyl-d9 (DHPC-d35), conditioned in chloroform or chloroform/methanol, were purchased from Avanti Polar Lipids (Alabaster, AL) and used without any further purification. D_2O, Tris-d11, and EDTA-d16 were from Eurisotop (Saint-Aubin, France). Chloroform or chloroform/methanol solutions containing the appropriate amounts of either zwitterionic (DMPC/DHPC, 1:1) or anionic (DMPC/DMPS/DHPC, 0.67:0.33:1) lipid mixtures were dried overnight under vacuum. The lipids were then rehydrated in TNE or deuterated-TNE (d-TNE) buffer solution (20 mM Tris-d11, 150 mM NaCl, and 0.1 mM EDTA-d16 (pD 7.5)) to reach a total lipid concentration of at least 200 mM. Then, the solution was frozen in liquid N_2, thawed (10 min at 40°C), vigorously shaken with a vortex (1 min), and then centrifuged (1.5 min, 6000 rotations per minute, MiniSpin; Eppendorf, Hamburg, Germany). This procedure was repeated twice to obtain a clear suspension of zwitterionic or anionic bicelles in hydrogenated or deuterated versions, denoted HZB/DZB and HAB/DAB, respectively. Stock solutions were diluted in TNE or d-TNE depending on the experiments.

The ideal bicelle model

The molar ratio of long/short-chain phospholipids is denoted q. It is the main parameter governing the size of the bicelles and is denoted q_{eff} (33,34) for effective molar ratio when the proportion of free DHPC is considered and is defined by Eq. 1:

$$q_{eff} = \frac{[LCP]}{[DHPC]_{total} - [DHPC]_{free}}, \quad (1)$$

where [LCP] is the concentration of long-chain phospholipids, i.e., DMPC and DMPS in our study, and [DHPC] is the concentration of short-chain phospholipids. The model proposed by Triba et al. (35), based on the volumes of the phospholipids, was used to estimate the radius and the MW of the bicelles by Eq. 2 (35,36):

$$R = r_{\perp} + \frac{r_{\perp} q_{eff}}{4\Lambda}\left[\pi + \left(\pi^2 + \frac{32\Lambda}{3q_{eff}}\right)^{1/2}\right], \quad (2)$$

where R is the radius of the bicelle, $r_{\perp}$ is the thickness of the rim (11 Å, the length of a DHPC molecule), and Λ is either the volume ratio of DHPC/DMPC (0.60) or to the weighted average volume of DMPC and DMPS (0.62). The molecular volumes of DMPC, DMPS, and DHPC are 1101 (37), 979 (38), and 660 (39) $Å^3$, respectively (see (14)).

Intrinsic tryptophan fluorescence

Fluorescence measurements were carried out on a Fluorolog spectrofluorometer (HORIBA Jobin-Yvon, Longjumeau, France). Tryptophan fluorescence emission spectra were recorded in low-volume quartz Hellma cells (120 μL) between 310 and 420 nm, using an excitation wavelength of 295 nm (bandwidth of 2 nm). Blanks corresponding to the buffer or bicelles alone were subtracted from the respective spectra. The protein concentration was 20 μM, and the total lipid concentration was 50 mM (~150 μM of bicellar objects). The measurement temperature was 26°C.

Microscale thermophoresis

Bicelles were labeled with 1 μM of 1,2-dioleoyl-sn-glycero-3-phospho-L-serine-N-(7-nitro-2-1,3-benzoxadiazol-4-yl) for a final concentration of 15 mM of lipids (~50 μM of bicellar objects) at q_{eff} = 1.3, and the [DMPC]/[DMPS] (mol/mol) ratio into the bilayer part was maintained equal to 2. The bicelles were titrated with a 0.75-fold serial dilution of R1–3 from 338 to 4.5 μM. The 16 solutions were then loaded into Monolith NT premium capillaries (NanoTemper, Munich, Germany), and thermophoresis was measured with a Monolith NT.115 instrument (NanoTemper). Instrument parameters were as follows: 30% LED power, 40% microscale thermophoresis (MST) power, and 5/30/5 laser off/on/off. Data were analyzed with the NT MO Affinity Analysis software v2.1.3 (NanoTemper). From the fit of the MST data, the concentration of the binding site ranges from 50 to 100 μM. Although close to the predicted number of bicelles according to the ideal bicelle model, this value can be affected by the bicelle aggregation number and by the value of q_{eff}. Indeed, working at 15 mM of lipids tends to be close to the $[DHPC]_{free}$ that could drastically affect q_{eff} even for a small misestimate of the total lipid concentration. The measurement temperature was 26°C.

Far-UV CD analysis

Far-ultraviolet (UV) circular dichroism (CD) spectra of the proteins were recorded on a Jasco (Easton, MD) J-815 spectropolarimeter from 200 to 240 nm in 0.02-cm pathlength Hellma cells. Blanks corresponding to the buffer or bicelles alone were subtracted from the respective spectra. The ratio of the ellipticity at 222–208 nm ($\theta_{222}/\theta_{208}$) was used as an indicator of the presence of a coiled coil (20,40). The protein concentration was 20 μM, and the total lipid concentration was 50 mM (~150 μM of bicellar objects). The measurement temperature was 26°C.

SANS experiments

Preparatory works were carried out with the KWS-2 instrument (at the Heinz Maier-Leibnitz Zentrum, Garching, Germany), and final investigations were done with the PACE (Laboratoire Léon Brillouin, Saclay, France), D22 (Institut Laue-Langevin, Grenoble), and KWS-1 (Heinz Maier-Leibnitz Zentrum, Garching) instruments. Two to three sample-to-detector distances were used with a wavelength varying from 4.7 to 7 Å

($\Delta\lambda/\lambda \sim 10\%$), to cover a Q range from 0.008 to 0.5 $Å^{-1}$ for the largest one, where $Q = \frac{4\pi \sin\theta}{\lambda}$ is the momentum transfer, λ is the wavelength, and 2θ is the scattering angle. All measurements were performed in 1-mm-thick Hellma Quartz Suprasil cells, and the intensities obtained are in absolute units (cm^{-1}). For SANS acquisitions, exactly the same buffer that had been used for bicelle rehydration was used to prepare protein/bicelle samples to guarantee a perfect buffer subtraction. The protein concentration was 103 μM (4.2 g/L), and the measurement temperature was 22°C, unless stated otherwise.

SANS data analysis

SANS data were analyzed with the ATSAS suite (41) and the Scatter software (http://www.bioisis.net/), following guidelines unless otherwise indicated. The PRIMUS software was used to determine the intensity at zero angle (I_0) and the radius of gyration (R_g). These values are defined at small Q-values ($QR_g < 0.8$–1.1) by the Guinier approximation with Eq. 3 (42):

$$I(Q) = I(0)exp\left(-\frac{Q^2R_g^2}{3}\right). \quad (3)$$

The apparent molecular weight (MW, in g • mol^{-1}) of the protein was estimated with Eq. 4 (43):

$$MW = \frac{I(0)N_A}{c(\Delta\rho V_P)^2}, \quad (4)$$

where $\Delta\rho$ (cm^{-2}) is the contrast (i.e., the difference in the neutron-scattering length densities) between R1–3 and d-TNE buffer, V_P is the partial specific volume ($cm^3 \cdot g^{-1}$) of the protein fragments, c is the protein concentration (g • cm^{-3}), and N_A is the Avogadro number (mol^{-1}). The V_P was determined from the density of the protein according to its amino acid sequence (http://psldc.isis.rl.ac.uk/Psldc/). Fitting procedures were performed using the SASview v3.1.0 software (http://www.sasview.org/). Bicelle data were fitted with the "core-shell cylinder" form factor model (44). The GNOM module from the ATSAS suite was used to determine the pair-distribution function $P(r)$, the maximal distance D_{max}, and the R_g in real space (denoted R_g^{real}) from $P(r)$. Twenty ab initio models were generated on ATSAS online (http://www.embl-hamburg.de/biosaxs/atsas-online/) with the DAMMIF software considering the data up to $Q = 0.25$ $Å^{-1}$. The models obtained were aligned and averaged with the DAMAVER software. The presented ab initio models correspond to the DAMMIF model with the smallest normalized spatial discrepancy surrounded by the corresponding DAMAVER model.

Click chemistry and liquid chromatography coupled with MS

HZB and HAB were labeled with 5% (mol/mol) of 1-palmitoyl-2-(9-(3-pent-4-ynyl-3-H-diazirin-3-yl)-nonanoyl)-sn-glycero-3-phosphocholine (pacFA PC) (Avanti Polar Lipids) bearing both photoactivable diazirine and clickable alkyne groups on one tail of the phospholipid (45). The modified bicelles were mixed with R1–3 to reach a final concentration of 50 mM of lipids and 15 μM of protein. Then, the protein/lipid complexes were exposed to ultraviolet A radiation (5 × 15 W, Stratalinker; GE Healthcare) for 5 min just before SDS-PAGE. The staining was performed using Coomassie blue (InstantBlue, Expedeon). The smeared parts of the gel, just above the band corresponding to R1–3, were cut into small pieces. Proteins contained in the gel pieces were reduced, alkylated, and then digested with trypsin (Promega, Madison, WI), and the resulting peptides were extracted as previously described (46). The peptide extract was loaded (10 μL) on a nano-high pressure liquid chromatography system (LC Packings Ultimate 3000, Dionex, Sunnyvale, CA) equipped with a trapping precolumn (5 mm × 300 μm internal diameter, 300 Å pore size, Pepmap C18, 5 μm, ThermoScientific, Waltham, MA) and an analytical column (15 cm × 75 μm internal diameter, 300 Å pore size, Pepmap C18, 5 μm, ThermoScientific). Reversed-phase separation was performed with the same gradient as described previously (47). Peptides were directly eluted from the nano-high pressure liquid chromatography column to the nanoelectrospray ion source of an LTQ-Orbitrap XL (ThermoScientific) mass spectrometer operating in data-dependent mode by automatically switching between full MS scan and MS/MS acquisitions on the 15 most intense precursor ions, as described previously (47). MS data were saved in the RAW file format with Xcalibur 2.0.7 and subjected to a database search for protein identification using Mascot Distiller 2.6.1.0 and Mascot Server 2.5.1 with its automatic decoy database search. The database searched contained the *E. coli* reference proteome from Uniprot (UP000000625, April 2017), the contaminants database from Mascot, and the sequence of the R1–3 protein fragment (785 sequences, 14,595,443 residues). Mass tolerance was set to 10 ppm for precursors and to 0.5 Da for fragments. Trypsin was selected as the enzyme, with two missed cleavages allowed. Protein modifications were fixed carbamidomethylation of cysteines and variable oxidation of methionine and variable pacFA PC. The pacFA PC modification ($C_{39}H_{72}NO_8P$, 713.4996 Da) was manually defined in the Mascot configuration editor with a neutral loss of phosphocholine ($C_5H_{14}NO_4P$, 183.066 Da). Because the photoactivation of diazirine forms carbene intermediates that can react with any amino acid side chain or peptide backbone, all amino acids were selected as possible modified sites. Proline Studio 1.4 was used for identification validation (peptide rank = 1, false discovery rate <1% at the peptide spectrum match level) (48). The mass spectrometry proteomics data have been deposited to the ProteomeXchange Consortium via the Proteomics Identification (49) partner repository with the data set identifier PXD007716 and 10.6019/PXD007716 (username: reviewer99373@ebi.ac.uk, password: gKQNG7SE).

CG-MD simulations

CG-MD simulations were run using the GROMACS 5.0 program (50) with the Martini CG force field (51,52). Two protein/lipid systems were simulated, i.e., the R1–3 dystrophin fragment with either hydrogenated zwitterionic bicelles (HZB) or hydrogenated anionic bicelles (HAB). The R1–3 model is from http://www.sasbdb.org/data/SASDB53/. In a manner similar to a previously improved protocol (53), bicelles ($q_{eff} = 1.3$) were built through the generation of a DMPC/DHPC or DMPC/DMPS/DHPC bilayer with the "insane" tool (54) by defining the number of lipids within the ideal bicelle model (35). This step was followed by a second step consisting of the enhancement of the size of the cubic simulation boxes up to 250 $Å^3$ by the addition of water and NaCl. All CG-MD simulations were performed at a constant temperature of 303 K and under NPT (constant number, pressure, and temperature) conditions. Final CG-MD trajectories of 20 μs were recorded and first analyzed by focusing on the period of relaxation of the lipid assembly and on the stability of the bicelle organization. Finally, the conversion of CG protein/lipid complexes to final atomic models was performed using the Backward tool (55). Theoretical SANS curves were generated with default parameters (except 50 harmonics) from 0.008 to 0.38 $Å^{-1}$ with the CRYSON program from the ATSAS suite. The theoretical curves were smeared using the "resolution file" according to the D22 instrument setup.

CG-IMD simulations

CG-IMD simulations were performed on the final R1–3/HAB model obtained from classical CG-MD using the GROMACS 5.0 implementation based on our previously published approach (56). Two different scenarios of coiled-coil opening were tested through five independent simulations for each. CG-IMD trajectories were recorded during 200 ps after checking

Please cite this article in press as: Dos Santos Morais et al., Human Dystrophin Structural Changes upon Binding to Anionic Membrane Lipids, Biophysical Journal (2018), https://doi.org/10.1016/j.bpj.2018.07.039

that the system returns well to equilibrium. A classical CG-MD of 2 ns was finally run from the open CG-IMD final model. Atomic reconstruction and theoretical SANS curves were processed as for classical CG-MD results.

RESULTS AND DISCUSSION

Protein and bicelle characterization

R1–3 dystrophin fragment described in Fig. 1 *A* was obtained with a high degree of purity, as assessed by SDS-PAGE analysis (Fig. S1 *A*). The molecular weight (MW) of R1–3 was determined by high-pressure size-exclusion chromatography coupled with multiangle light scattering (HPSEC-MALS) (Fig. S1 *B*). The obtained MW of 38.2 ± 0.4 kDa is in line with the expected values of 38.5 kDa, assessing the monomeric state of R1–3 (Fig. S1 *B*). The quality control of the bicelles was assessed by NMR, HPSEC-dynamic light scattering, HPSEC-MALS (Fig. S1, *C–E*), and SANS (Fig. S2, *A* and *B*). All these allowed us to conclude that both R1–3 and bicelles exhibit the expected sizes and monodispersity and therefore can be further used for the characterization of protein/lipid interactions.

Protein structure changes upon binding to bicelles

The protein/bicelle interactions were highlighted by tryptophan (Trp) intrinsic fluorescence variation, attributed to a modification in the Trp environment due to lipid binding. As expected, Trp intrinsic fluorescence of R1–3 in the presence of HZB or HAB increases significantly (Fig. 2 *A*). To go deeper into the characterization of the protein/bicelle interactions, MST was used to determine the dissociation constant (K_d) of the complexes, which are in the range of 10 μM for both R1–3/HZB and R1–3/HAB (Fig. 2 *B*). Finally, CD was used to probe the potential secondary structure modifications of the protein during its interactions with both types of bicelles (Fig. 2 *C*). The CD spectrum of R1–3 alone is typical of an overall α-helical folding with the presence of two minima at 222 and 208 nm. These data confirm that R1–3 is properly folded (18,20). For R1–3 in the presence of HZB or HAB, although the α-helical folding is globally preserved during the interaction with both types of bicelles, a partial loss of helicity occurs. The 3D structure of R1–3 was first analyzed by SANS in the absence of bicelles (Fig. 2 *D*). The measured MW (56 kDa) and radius of gyration (R_g, 42 ± 1 Å) are in good agreement with a monomeric state of the protein and consistent with HPSEC-MALS data. The pair-distance distribution $P(r)$ is typical of an elongated protein with a peak observed at ~20 Å and a smooth fall to D_{max} at 177 Å (Fig. 2 *E*). The R_g^{real} value of 43 Å is consistent with the above Guinier analysis. We recorded SANS data of R1–3 at exactly the same concentration as for the protein free in solution, but in the presence of zwitterionic or anionic (57) bicelles in deuterated version (DZB and DAB, respectively), which can be contrast matched in 100% d-TNE buffer (14,57) (Fig. S2 *B*, *inset*). The disk-shaped morphology of bicelles is supported by the fit of the SANS data obtained at 42% d-TNE buffer, and this morphology of the bicelles is preserved in R1–3/DZB and R1–3/DAB complexes (Fig. S2, *B–C*). This result discards the unlikely scenario in which R1–3 would be located inside the bilayer part of the bicelles.

For the R1–3/DZB complex, the SANS signal is different from that of the protein alone, but R_g (41 ± 1 Å) and D_{max} (178 Å) remain constant (Fig. 2, *D–E*). We conclude that either the tertiary structure of R1–3 is maintained in the presence of zwitterionic bicelles or a change, if any, is not large enough to be detectable by SANS. Surprisingly, for R1–3 in interaction with anionic bicelles, R_g (60 ± 4 Å) and D_{max} (248 Å) are significantly larger. Such increases indicate a large and significant elongation of the tertiary structure of R1–3 when bound to anionic bicelles. The generated ab initio models support this conclusion, showing more extended low-resolution envelopes of R1–3 when bound to DAB compared to the envelopes found for the protein free in solution or in interaction with DZB (Figs. 2 *D*, *inset*).

Moreover, Kratky and Porod-Debye SANS plots confirmed the well-folded and compact states of R1–3 (Fig. S3) in any cases. Finally, the calculated apparent MWs (~45 kDa) in the presence of both types of bicelles exclude the possibility of the dimerization upon lipid binding. The structural parameters and the shape-model fitting results are summarized in Table S1 and have been deposited at the SASBDB database (58,59) with the accession codes of SASDDJ9, SASDDK9, and SASDDL9 for R1–3 alone or in interaction with zwitterionic or anionic phospholipid bicelles, respectively.

Opening of repeat 1 when R1–3 is bound to anionic bicelles

The interactions of R1–3 with both types of bicelles were more deeply studied by CG-MD experiments. The radial distribution function of the lipids indicates that all simulations report stable self-organized bicelles after 20–30 ns of CG-MD, a long time before the 440–320 ns recruitment of the protein fragment observed for R1–3/HZB and R1–3/HAB complexes, respectively (Fig. S4, *A* and *B*). R1–3/HZB and R1–3/HAB CG models, obtained after 20 μs of MD simulation, were considered reliable because the relative deviation of the protein particle positions remains globally stable during the last half of the trajectories (Fig. S4, *C* and *D*). Surprisingly, in both simulations, R1–3 is spontaneously recruited to the bicelle surface at its torus part (Fig. 3 *A*), which presents a high level of lipid packing defect whatever the nature of the bicelle. To check these

Please cite this article in press as: Dos Santos Morais et al., Human Dystrophin Structural Changes upon Binding to Anionic Membrane Lipids, Biophysical Journal (2018), https://doi.org/10.1016/j.bpj.2018.07.039

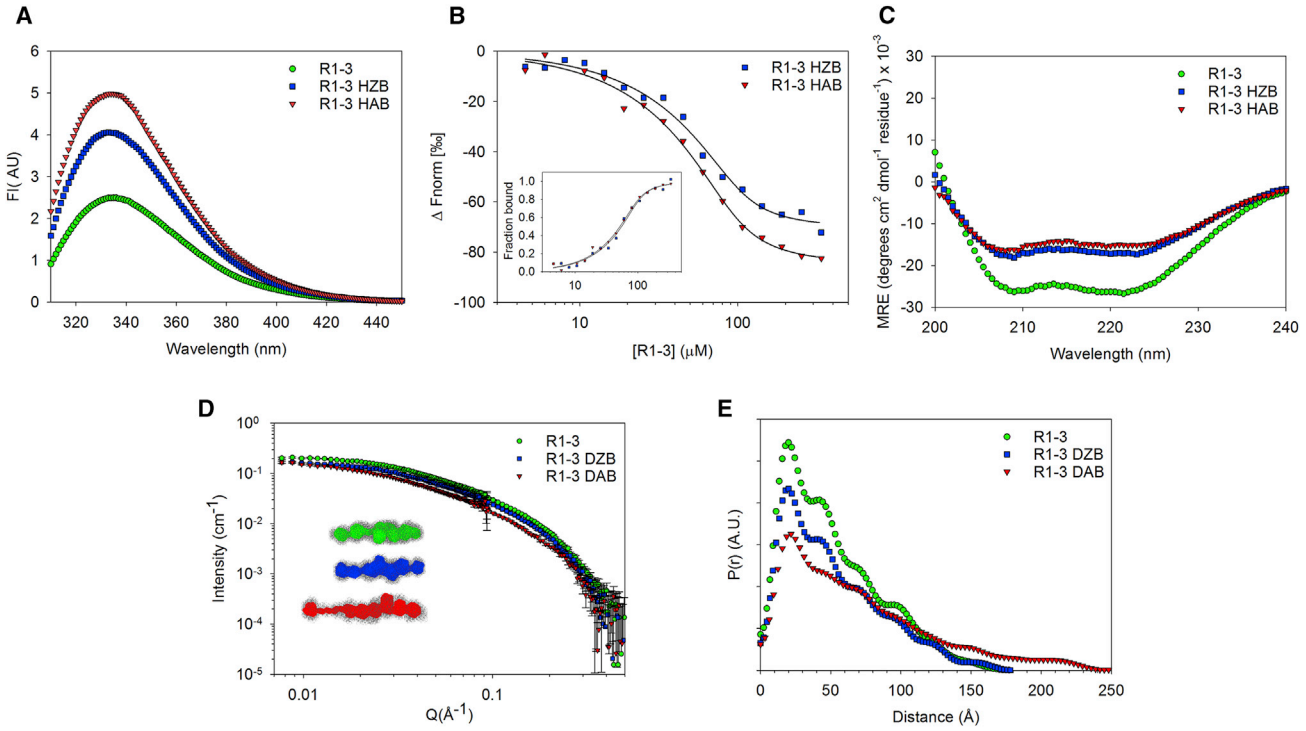

Web 3C

FIGURE 2 Characterization of the protein/lipid interactions of the R1–3 dystrophin fragment. (*A*) The Trp fluorescence intensity of R1–3 in the absence (*green circles*) or in the presence of zwitterionic (HZB, *blue squares*) or anionic (HAB, *red triangles*) bicelles is shown. (*B*) MST data is shown; the dissociation constant (K_d) was determined to be ~10 μM for the protein/bicelle complex. The inset shows the same MST data but using the "fraction bound versus protein concentration" representation. (*C*) Far-UV CD spectra with the same legend as for fluorescence intensity are shown. CD spectra highlight that the α-helical folding of R1–3 is maintained upon lipid binding. (*D*) SANS intensities measured for R1–3 alone in solution (*green circles*) or in interaction with contrast-matched deuterated zwitterionic (DZB, *blue squares*) or anionic (DAB, *red triangles*) bicelles are shown. The inset shows ab initio shapes of (from *top* to *bottom*) R1–3 free in solution (*green*) or in interaction with DZB (*blue*) or DAB (*red*), corresponding to the DAMMIF models obtained with the smallest normalized spatial discrepancy and surrounded by the corresponding DAMAVER model (*gray*). (*E*) The pair-distribution function $P(r)$ analysis with the same color code showing an increase of D_{max} of R1–3 when the protein fragment is in interaction with anionic bicelles is shown. To see this figure in color, go online.

in silico results experimentally, we labeled the bicelles with a bifunctional phospholipid (45) (pacFA PC) (Fig. S5 *A*). The cross-link reaction (Fig. S5, *B* and *C*) should occur only if R1–3 is close to this diazirin group, i.e., if R1–3 is located at the bicelle torus, as suggested by CG-MD data. Three peptides of R1–3 linked to the phospholipid were identified by MS (Figs. S5 *D* and S6, *A–C*; Table S2), corresponding to the protein/lipid interaction areas suggested by CG-MD located in the R1 and R3 repeats (Fig. 3 *A*) for both types of bicelles. Transmission electron microscopy analysis of the R1–3/HAB complex highlights that R1–3 is found at the torus of the bicelles (Fig. S6 *D*). All together, these results provide evidences concerning both the localization of R1–3 at the torus of the bicelles and an accurate mapping of the protein/lipid interactions at the R1 and R3 coiled-coil repeats of the R1–3 dystrophin fragment.

The CG-MD data set for R1–3/HAB was chosen for further investigation by CG-IMD to understand such conformational modification. An opening of the coiled coil could explain the R_g and D_{max} increase of R1–3 obtained in the corresponding SANS experiments, as well as the extended ab initio envelope. Moreover, the opening of the coiled coil at one of the two extremities (R1 or R3) could support MS mapping, discarding the R2 opening. CG-IMD simulations enabled the opening of the dystrophin coiled coil thanks to a force applied interactively during CG-MD on the R1–3/HAB system. Modeling an extended protein in line with the SANS data was achieved through two CG-IMD scenarios (Fig. S7, *A* and *B*; Video S1). Five all-atom models were generated (Fig. 3 *C*) and compared with the experimental data. Among them, the model having the best overall agreement with MS contact mapping (Fig. S7, *C–E*), a suitable R_g (59 Å), and the best fit of the SANS data (lowest χ^2 value) was considered the most reliable structural model for R1–3 interacting with an anionic bicelle (Fig. 3 *D*), namely opening the 1HA-1HB helices of the R1 repeat. This opening may be necessary for the membrane anchoring of dystrophin into the curved parts (22) of the sarcolemma to firmly support the membrane of muscle cells during the muscle elongation/contraction process (this R1–3 all-atom model is accessible with the SASDDL9 code).

Please cite this article in press as: Dos Santos Morais et al., Human Dystrophin Structural Changes upon Binding to Anionic Membrane Lipids, Biophysical Journal (2018), https://doi.org/10.1016/j.bpj.2018.07.039

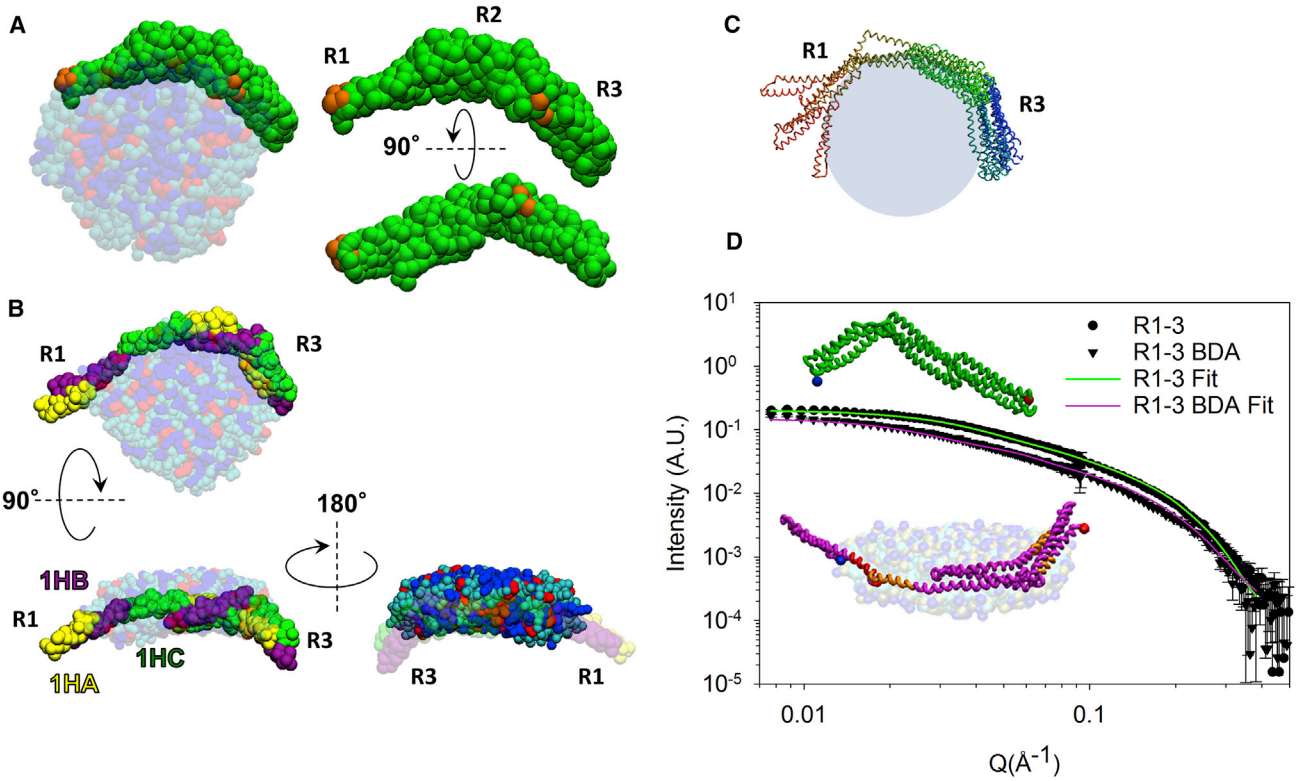

Web 3C

FIGURE 3 (*A*) Final structural model obtained by CG-MD of R1–3 bound to anionic bicelles (HAB). The protein is shown in green, with orange spots corresponding to the pacFA PC cross-linked regions identified by MS. Lipids are colored in blue for DMPC, red for DMPS, and cyan for DHPC. (*B*) The final structural model obtained by CG-IMD for the R1–3/anionic bicelle complex is shown; HA, HB, and HC helices of each repeat are shown in yellow, purple, and green, respectively. (*C*) A collection of the five protein all-atom models obtained after opening the 1HA and 1HB helical regions of the R1 repeat through CG-IMD simulations is shown. (*D*) Experimental SANS intensities (*circles* and *triangles* for R1–3 alone or bound to contrast-matched anionic bicelles, respectively) are shown fitted with the theoretical CRYSON curves generated from the R1–3 model free in solution (*green*) and the R1–3 model bound to anionic bicelles (*purple*). The inset shows the corresponding all-atom models represented with the same color code. Blue and red dots represent the N- and C-termini, respectively. The peptides bearing the pacFA PC are colored in orange, and the putative ALPS motif (QGRVGNILQLGSKLIGTG) is colored in red. To see this figure in color, go online.

Several peripheral proteins recognize lipid-packing defects by adsorbing preferentially to positively curved membranes through the insertion of amphipathic sequences (60). Interestingly, based on sequence similarity, a putative amphipathic lipid-packing sensor (ALPS) motif was found in the 1HB helix of the R1 repeat of human dystrophin (61) that we found to open during the interaction with anionic bicelles. This putative ALPS motif is always in contact with the bicelle (Fig. S8). In line with the literature (60), the preference of the ALPS motif of dystrophin for the torus part of the bicelle is likely related to a hydrophobic interaction rather than an electrostatic one because the contact frequencies with tails are higher compared to heads (Fig. S8). Finally, it has been suggested that in helical ALPS motifs, hydrophobic residues, once inserted, stabilize large lipid-packing defects by filling them; the molecular details of the interaction between these motifs and biological membranes, however, remain elusive (60). In this case, it is reasonable to hypothesize that such a behavior could be involved in the native dystrophin/lipid interaction. Nevertheless, understanding how the specific amino acid composition of the 1HB helix of the R1 repeat might recognize and stabilize the lipid-packing defects at the torus of the bicelle requires additional work.

CONCLUSIONS

We characterized the protein/lipid interactions of R1–3 protein fragment from the central domain of dystrophin, a protein involved in severe genetic diseases. Obtaining structural information about the central domain of this peripheral membrane protein, free in solution or in the presence of lipids, is not accessible by x-ray crystallography and/or NMR. We highlight by MST that R1–3 interacts with zwitterionic bicelles and even more with anionic bicelles. By using the contrast-matched bicelle tool (14) in a SANS approach, we demonstrate that R1–3 undergoes large conformational modifications when bound to bicelles containing anionic phospholipids. We used click chemistry and MS coupled with in silico CG-MD to determine a reliable mapping of the R1–3/lipid interactions. Finally, using the innovative CG-IMD method, we propose a relevant

Please cite this article in press as: Dos Santos Morais et al., Human Dystrophin Structural Changes upon Binding to Anionic Membrane Lipids, Biophysical Journal (2018), https://doi.org/10.1016/j.bpj.2018.07.039

and to our knowledge new all-atom model of R1–3 in interaction with anionic bicelles, providing evidence that the R1 first repeat of the dystrophin central domain undergoes an opening of its coiled-coil structure. This opening may be necessary for the membrane anchoring of dystrophin into the sarcolemma to firmly support the plasma membrane of muscle cells during the muscle elongation/contraction process. Therefore, our work may contribute to the design of rationalized mini-dystrophins as a gene therapy for the treatment of Duchenne muscular dystrophy patients.

Finally, in addition to their use in the SANS contrast variation technique, we demonstrate that bicelles are a versatile tool usable in MST, HPSEC-MALS, and CG-IMD. Therefore, our approaches can confidently be employed for the characterization of protein/lipid interactions, as well as the structural analysis of other peripheral and even integral membrane proteins incompatible with high resolution structural methods.

SUPPORTING MATERIAL

Supporting Materials and Methods, eight figures, two tables, and one video are available at http://www.biophysj.org/biophysj/supplemental/S0006-3495(18)30934-2.

AUTHOR CONTRIBUTIONS

R.D.S.M., O.D., J.P., E.L.R., S.C., and J.-F.H. designed the study. R.D.S.M., A.C., T.C. prepared the samples. R.D.S.M., O.D., D.M.-L., M.L., A.M., A.-E.M., C.R.-N., A.B., M.-S.A., and S.C. acquired the data. R.D.S.M., O.D., D.M.-L., M.L., S.C., and J.-F.H. analyzed and/or interpreted the data. R.D.S.M., O.D., S.C., and J.-F.H. wrote the manuscript. All authors reviewed the manuscript and approved the final version.

ACKNOWLEDGMENTS

Q2 We thank C. Tascon (CPR, UMR-CNRS 6290), A. Burel (MRic platform), and NMR PRISM platform and the Spectroscopies-DCTP core facility from BIOSIT at the University of Rennes 1, as well as G. David and B. Pineau (SOLEIL).

We thank AFM-Telethon (#18211), the Conseil Régional de Bretagne (ARED #8893), Laboratoire Léon Brillouin, and SOLEIL (theses #2014) for funding. LLB, ILL, and JCNS neutron facilities are acknowledged for beamtime on PACE, D22, KWS-1, and KWS-2, as well as the GENCI program.

REFERENCES

1. Seddon, A. M., P. Curnow, and P. J. Booth. 2004. Membrane proteins, lipids and detergents: not just a soap opera. *Biochim. Biophys. Acta.* 1666:105–117.
2. Hendrickson, W. A. 2016. Atomic-level analysis of membrane-protein structure. *Nat. Struct. Mol. Biol.* 23:464–467.
3. Fernandez-Leiro, R., and S. H. Scheres. 2016. Unravelling biological macromolecules with cryo-electron microscopy. *Nature.* 537:339–346.
4. Petoukhov, M. V., and D. I. Svergun. 2007. Analysis of X-ray and neutron scattering from biomacromolecular solutions. *Curr. Opin. Struct. Biol.* 17:562–571.
5. Pérez, J., and A. Koutsioubas. 2015. Memprot: a program to model the detergent corona around a membrane protein based on SEC-SAXS data. *Acta Crystallogr. D Biol. Crystallogr.* 71:86–93.
6. Koutsioubas, A. 2017. Low-resolution structure of detergent-solubilized membrane proteins from small-angle scattering data. *Biophys. J.* 113:2373–2382.
7. Heller, W. T. 2010. Small-angle neutron scattering and contrast variation: a powerful combination for studying biological structures. *Acta Crystallogr. D Biol. Crystallogr.* 66:1213–1217.
8. Le Cœur, C., S. Combet, …, S. Longeville. 2015. Conformation of the poly(ethylene Glycol) chains in DiPEGylated hemoglobin specifically probed by SANS: correlation with PEG length and in vivo efficiency. *Langmuir.* 31:8402–8410.
9. Gabel, F. 2015. Small-angle neutron scattering for structural biology of protein-RNA complexes. *Methods Enzymol.* 558:391–415.
10. Sonntag, M., P. K. A. Jagtap, …, M. Sattler. 2017. Segmental, domain-selective perdeuteration and small-angle neutron scattering for structural analysis of multi-domain proteins. *Angew. Chem. Int.Engl.* 56:9322–9325.
11. Breyton, C., F. Gabel, …, C. Ebel. 2013. Small angle neutron scattering for the study of solubilised membrane proteins. *Eur. Phys. J. E Soft Matter.* 36:71.
12. Naing, S. H., R. C. Oliver, …, R. L. Lieberman. 2018. Solution structure of an intramembrane aspartyl protease via small angle neutron scattering. *Biophys. J.* 114:602–608.
13. Midtgaard, S. R., T. A. Darwish, …, L. Arleth. 2018. Invisible detergents for structure determination of membrane proteins by small-angle neutron scattering. *FEBS J.* 285:357–371.
14. Dos Santos Morais, R., O. Delalande, …, S. Combet. 2017. Contrast-matched isotropic bicelles: a versatile tool to specifically probe the solution structure of peripheral membrane proteins using SANS. *Langmuir.* 33:6572–6580.
15. Le Rumeur, E., S. J. Winder, and J. F. Hubert. 2010. Dystrophin: more than just the sum of its parts. *Biochim. Biophys. Acta.* 1804:1713–1722.
16. Monaco, A. P., R. L. Neve, …, L. M. Kunkel. 1986. Isolation of candidate cDNAs for portions of the Duchenne muscular dystrophy gene. *Nature.* 323:646–650.
17. Stark, A. E. 2015. Determinants of the incidence of Duchenne muscular dystrophy. *Ann. Transl. Med.* 3:287.
18. Legardinier, S., J. F. Hubert, …, E. Le Rumeur. 2008. Sub-domains of the dystrophin rod domain display contrasting lipid-binding and stability properties. *Biochim. Biophys. Acta.* 1784:672–682.
19. Zhao, J., K. Kodippili, …, Y. Lai. 2016. Dystrophin contains multiple independent membrane-binding domains. *Hum. Mol. Genet.* 25:3647–3653.
20. Legardinier, S., C. Raguénès-Nicol, …, E. Le Rumeur. 2009. Mapping of the lipid-binding and stability properties of the central rod domain of human dystrophin. *J. Mol. Biol.* 389:546–558.
21. Vié, V., S. Legardinier, …, E. Le Rumeur. 2010. Specific anchoring modes of two distinct dystrophin rod sub-domains interacting in phospholipid Langmuir films studied by atomic force microscopy and PM-IRRAS. *Biochim. Biophys. Acta.* 1798:1503–1511.
22. García-Pelagio, K. P., R. J. Bloch, …, H. González-Serratos. 2011. Biomechanics of the sarcolemma and costameres in single skeletal muscle fibers from normal and dystrophin-null mice. *J. Muscle Res. Cell Motil.* 31:323–336.
23. Legrand, B., E. Giudice, …, E. Le Rumeur. 2011. Computational study of the human dystrophin repeats: interaction properties and molecular dynamics. *PLoS One.* 6:e23819.
24. Chamberlain, J. R., and J. S. Chamberlain. 2017. Progress toward gene therapy for Duchenne muscular dystrophy. *Mol. Ther.* 25:1125–1131.
25. Le Guiner, C., L. Servais, …, G. Dickson. 2017. Long-term microdystrophin gene therapy is effective in a canine model of Duchenne muscular dystrophy. *Nat. Commun.* 8:16105.

26. Delalande, O., A. E. Molza, …, E. Le Rumeur. 2018. Dystrophin's central domain forms a complex filament that becomes disorganized by in-frame deletions. *J. Biol. Chem.* 293:6637–6646.

27. Fiehn, W., J. B. Peter, …, M. Gan-Elepano. 1971. Lipids and fatty acids of sarcolemma, sarcoplasmic reticulum, and mitochondria from rat skeletal muscle. *J. Biol. Chem.* 246:5617–5620.

28. Leventis, R., and J. R. Silvius. 2010. Quantitative experimental assessment of macromolecular crowding effects at membrane surfaces. *Biophys. J.* 99:2125–2133.

29. Nagatomo, T., M. Sasaki, and T. Konishi. 1984. Differences in lipid composition and fluidity of cardiac sarcolemma prepared from newborn and adult rabbits. *Biochem. Med.* 32:122–131.

30. Leventis, P. A., and S. Grinstein. 2010. The distribution and function of phosphatidylserine in cellular membranes. *Annu. Rev. Biophys.* 39:407–427.

31. Winder, S. J., T. J. Gibson, and J. Kendrick-Jones. 1995. Dystrophin and utrophin: the missing links! *FEBS Lett.* 369:27–33.

32. Sarkis, J., J. F. Hubert, …, V. Vié. 2011. Spectrin-like repeats 11-15 of human dystrophin show adaptations to a lipidic environment. *J. Biol. Chem.* 286:30481–30491.

33. Beaugrand, M., A. A. Arnold, …, I. Marcotte. 2014. Lipid concentration and molar ratio boundaries for the use of isotropic bicelles. *Langmuir.* 30:6162–6170.

34. Glover, K. J., J. A. Whiles, …, R. R. Vold. 2001. Structural evaluation of phospholipid bicelles for solution-state studies of membrane-associated biomolecules. *Biophys. J.* 81:2163–2171.

35. Triba, M. N., D. E. Warschawski, and P. F. Devaux. 2005. Reinvestigation by phosphorus NMR of lipid distribution in bicelles. *Biophys. J.* 88:1887–1901.

36. Mineev, K. S., K. D. Nadezhdin, …, A. S. Arseniev. 2016. Characterization of small isotropic bicelles with various compositions. *Langmuir.* 32:6624–6637.

37. Petrache, H. I., S. Tristram-Nagle, and J. F. Nagle. 1998. Fluid phase structure of EPC and DMPC bilayers. *Chem. Phys. Lipids.* 95:83–94.

38. Petrache, H. I., S. Tristram-Nagle, …, J. F. Nagle. 2004. Structure and fluctuations of charged phosphatidylserine bilayers in the absence of salt. *Biophys. J.* 86:1574–1586.

39. Small, D. M. 1986. The Physical Chemistry of Lipids: From Alkanes to Phospholipids. Plenum Press, New York, p. 672.

40. Mehboob, S., B. H. Luo, …, L. W. Fung. 2001. alpha beta spectrin coiled coil association at the tetramerization site. *Biochemistry.* 40:12457–12464.

41. Franke, D., M. V. Petoukhov, …, D. I. Svergun. 2017. *ATSAS 2.8*: a comprehensive data analysis suite for small-angle scattering from macromolecular solutions. *J. Appl. Cryst.* 50:1212–1225.

42. Glatter, O., and O. Kratky. 1982. Small Angle X-ray Scattering. Academic Press, London, UK.

43. Jeffries, C. M., M. A. Graewert, …, D. I. Svergun. 2016. Preparing monodisperse macromolecular samples for successful biological small-angle X-ray and neutron-scattering experiments. *Nat. Protoc.* 11:2122–2153.

44. Kline, S. R. 2006. Reduction and analysis of SANS and USANS data using IGOR Pro. *J. Appl. Cryst.* 39:895–900.

45. Haberkant, P., R. Raijmakers, …, J. C. Holthuis. 2013. In vivo profiling and visualization of cellular protein-lipid interactions using bifunctional fatty acids. *Angew. Chem. Int.Engl*. 52:4033–4038.

46. Lavigne, R., E. Becker, …, C. Pineau. 2012. Direct iterative protein profiling (DIPP) - an innovative method for large-scale protein detection applied to budding yeast mitosis. *Mol. Cell. Proteomics.* 11:M111.012682.

47. Jumeau, F., E. Com, …, C. Pineau. 2015. Human spermatozoa as a model for detecting missing proteins in the context of the chromosome-centric human proteome project. *J. Proteome Res.* 14:3606–3620.

48. Carapito, C., L. Lane, …, Y. Vandenbrouck. 2015. Computational and mass-spectrometry-based workflow for the discovery and validation of missing human proteins: application to chromosomes 2 and 14. *J. Proteome Res.* 14:3621–3634.

49. Vizcaíno, J. A., A. Csordas, …, H. Hermjakob. 2016. 2016 update of the PRIDE database and its related tools. *Nucleic Acids Res.* 44:D447–D456.

50. Hess, B., C. Kutzner, …, E. Lindahl. 2008. GROMACS 4: algorithms for highly efficient, load-balanced, and scalable molecular simulation. *J. Chem. Theory Comput.* 4:435–447.

51. Marrink, S. J., H. J. Risselada, …, A. H. de Vries. 2007. The MARTINI force field: coarse grained model for biomolecular simulations. *J. Phys. Chem. B.* 111:7812–7824.

52. Monticelli, L., S. K. Kandasamy, …, S. J. Marrink. 2008. The MARTINI coarse-grained force field: extension to proteins. *J. Chem. Theory Comput.* 4:819–834.

53. Vácha, R., and D. Frenkel. 2014. Stability of bicelles: a simulation study. *Langmuir.* 30:4229–4235.

54. Wassenaar, T. A., H. I. Ingólfsson, …, S. J. Marrink. 2015. Computational lipidomics with insane: a versatile tool for generating custom membranes for molecular simulations. *J. Chem. Theory Comput.* 11:2144–2155.

55. Wassenaar, T. A., K. Pluhackova, …, D. P. Tieleman. 2014. Going backward: a flexible geometric approach to reverse transformation from coarse grained to atomistic models. *J. Chem. Theory Comput.* 10:676–690.

56. Delalande, O., N. Férey, …, M. Baaden. 2009. Complex molecular assemblies at hand via interactive simulations. *J. Comput. Chem.* 30:2375–2387.

57. Struppe, J., J. A. Whiles, and R. R. Vold. 2000. Acidic phospholipid bicelles: a versatile model membrane system. *Biophys. J.* 78:281–289.

58. Trewhella, J., A. P. Duff, …, A. E. Whitten. 2017. 2017 publication guidelines for structural modelling of small-angle scattering data from biomolecules in solution: an update. *Acta Crystallogr. D Struct. Biol.* 73:710–728.

59. Valentini, E., A. G. Kikhney, …, D. I. Svergun. 2015. SASBDB, a repository for biological small-angle scattering data. *Nucleic Acids Res.* 43:D357–D363.

60. Vanni, S., L. Vamparys, …, B. Antonny. 2013. Amphipathic lipid packing sensor motifs: probing bilayer defects with hydrophobic residues. *Biophys. J.* 104:575–584.

61. Drin, G., J. F. Casella, …, B. Antonny. 2007. A general amphipathic α-helical motif for sensing membrane curvature. *Nat. Struct. Mol. Biol.* 14:138–146.